INFORMATION TO USERS

This manuscript has been reproduced from the microfilm master. UMI films the text directly from the original or copy submitted. Thus, some thesis and dissertation copies are in typewriter face, while others may be from any type of computer printer.

The quality of this reproduction is dependent upon the quality of the copy submitted. Broken or indistinct print, colored or poor quality illustrations and photographs, print bleedthrough, substandard margins, and improper alignment can adversely affect reproduction.

In the unlikely event that the author did not send UMI a complete manuscript and there are missing pages, these will be noted. Also, if unauthorized copyright material had to be removed, a note will indicate the deletion.

Oversize materials (e.g., maps, drawings, charts) are reproduced by sectioning the original, beginning at the upper left-hand corner and continuing from left to right in equal sections with small overlaps. Each original is also photographed in one exposure and is included in reduced form at the back of the book.

Photographs included in the original manuscript have been reproduced xerographically in this copy. Higher quality 6" x 9" black and white photographic prints are available for any photographs or illustrations appearing in this copy for an additional charge. Contact UMI directly to order.

UMI

A Bell & Howell Information Company
300 North Zeeb Road, Ann Arbor MI 48106-1346 USA
313/761-4700 800/521-0600

Nuclear Transport Phenomena in the Reactions ^{112}Sn+^{48}Ca and ^{112}Sn+^{40}Ca at E/A=35 MeV

by

Dileep Kumar Agnihotri

Submitted in Partial Fulfillment
of the
Requirements for the Degree

Doctor of Philosophy

Supervised by
Wolf Udo Schröder
Professor of Chemistry

Department of Chemistry
The College
Arts and Sciences
University of Rochester
Rochester, New York
1998

UMI Number: 9916576

UMI Microform 9916576
Copyright 1999, by UMI Company. All rights reserved.

This microform edition is protected against unauthorized
copying under Title 17, United States Code.

UMI
300 North Zeeb Road
Ann Arbor, MI 48103

This work is dedicated to

my parents.

Curriculum Vitae

The author was born in 1969 at Farrukhabad, UP, India. He completed his secondary and higher secondary education from K.V. Fatehgarh, in 1986. He attended Agra University, Agra, India, from 1986 to 1990 and graduated with a Master of Science degree in physics, with specialization in electronics. During his college, he was awarded state scholarship of Uttar Pradesh, India. Later in 1990, he joined Nuclear Science Center (NSC), New Delhi, India, as a research fellow. After a year of training in the field of accelerator based heavy-ion research at NSC laboratory, he joined Department of Physics, Panjab University, Chandigarh, India, and conducted research for two years on a project "Fusion reactions at high excitation and large angular momentum". During this period (1991-1993) he was awarded a fellowship from the University Grant Commission of India (UGC).

In September 1993, author came to University of Rochester to pursue his research in Nuclear Chemistry with Professor W. U. Schröder. He performed his experiments at National Superconducting Cyclotron Laboratory (NSCL), Michigan State University, East Lansing, USA. In addition, he pursued his graduate studies in Nuclear Chemistry in the Department of Chemistry, University of Rochester, and also participated in the teaching program at university. During this tenure, he held positions of research assistant (September 1993 - November 1998) and teaching assistant (September 1996 - May 1998). He received the Master of Science degree in 1997 in Physical Chemistry. He continued his research in Nuclear Chemistry while preparing this dissertation for the degree of Doctor of Philosophy. He was awarded the "Sherman Clark Fellowship" for the academic years 1997 and 1998. During the course of this research, he was supported by a grant from the United States Department of Energy.

Acknowledgments

First, I would like to thank my thesis advisor W. U. Schröder, Professor of Chemistry, University of Rochester. His valuable advises, enthusiasm, lengthy discussions on the subject, and critical comments on my research work, helped tremendously in bringing this work to a successful completion. In addition, I would like to thank Dr. J. Tōke, a member of my research group, who helped me learn many aspects related to my research. Throughout the course of this work, his humor, suggestions, and insightful discussions made this work very enjoyable. I am also very thankful to other members that encompass my research group, Dr. B. Djerroud, Dr. W. Skulksi, Dr. S. Baldwin, K. Wyrozebski and D. Kostecke for their assistance and help during this work. Ms. E. Katta developed the anti-coincidence counters for the experiments. I would like to thank Prof. D. Cline, Ms. Eileen Pullara and D. Munson (computer support), of the Nuclear Science Research Laboratory (NSRL), for their help and support.

I would like to thank my collaborators from Indiana University, Indiana, Prof. R. T. Desouza, B. Davin and Dr. E. Cornell for their active interest in this project. A set of detectors for my experiments were provided by these collaborators from Indiana. I would also like to thank the National Superconducting Cyclotron Laboratory (NSCL), Michigan State University, Michigan, and its crew members for providing a high quality beam to carry out my thesis experiments. It is my pleasure to mention the names of Prof. N. Anataraman, Dr. R. Ronningen, Dr. D. Sanderson, J. Stetson and R. Fox for providing all possible assistance during the experiments at NSCL.

I would like extend my thanks to Prof. G. K. Mehta, Director, Nuclear Science Center (NSC), New Delhi, for giving me an opportunity to begin my research career in the field of Nuclear Science. I admire his dedication and hard work in establishing a world class research facility in Delhi. I thank Dr. S. K. Datta, Dr. R. K. Bhowmik, Dr. A. Roy, Dr. A. K. Sinha and Dr. D. K. Avasthi for their valuable guidance and encouraging discussions during my training and experiments at NSC. I would also like to thank my friends and former colleagues at NSC and Panjab University Chandigarh, Dr. M. J. Singh, Dr. A. Kumar, Dr. V. Ravi Kumar, Dr. S. S. Ghugre, Dr. V. Kumar, Dr. N.V.S.V. Prasad, Dr. I. Majumdar, Dr. S.K. Mandal, Dr. D. Mehta, Dr. J. Goswami, Dr. P. Rana, Dr. S. Kumar, Dr. K.P. Singh, Dr. K.C. Jain, Dr. A. Sharma, Dr. R. Dogra, Dr. A. C. Katoch, P. Sharma, R. Singh, P. Batham, D. Pattanaik and K. K. Chadda, for providing a close knitted family environment.

In the end, I would like to express my gratitude to my parents and family members for all of their support and patience in bearing my absence from home for so many years. A special heartfelt thanks to my wife Dipti for her love, support, and encouragement through all the good and bad times. Finally, I dedicate this work to my parents.

This work was supported by the US Department of Energy under grant number DE-FG02-88ER40414.

Abstract

An exclusive study has been performed of the reactions ^{112}Sn + ^{48,40}Ca at E/A = 35MeV. Probabilities and emission patterns of associated light particles (neutrons and protons), as well as the charge distributions of projectile-like fragments (PLF), are used to probe nuclear transport phenomena in the Fermi-energy domain. Correlations between PLF deflection angle and dissipated energy, the reaction yields, and PLF Z distributions are interpreted in terms of the reaction dynamics. The emission of non-equilibrium particles is compared to the theoretical models, and their role in limiting the energy dissipation is explored.

The PLF deflection functions demonstrate dissipative orbiting for both reactions. Calculations with the nucleon exchange model (NEM) qualitatively reproduce experimental PLF angular distributions and average correlations between atomic number and kinetic energy. The neutrons and protons emitted in both reactions stem dominantly from the statistical decay of primary reaction fragments. Their yields illustrate the relaxation of excitation energy and mass-to-charge density, although no degree of freedom is completely equilibrated. Distinct components of non-equilibrium particles with a rather hard energy spectra are observed. Up to 25% of the dissipated entrance-channel energy can be carried away by such particles, limiting thermal excitation of the system.

Yields and emission patterns of the non-equilibrium neutrons and protons reveal approximate symmetry and random emission in the nucleon-nucleon rest frame. However, the flow of these non-equilibrium particles is more neutron rich than either target or projectiles, indicating the importance of the nuclear surface. With increasing energy loss, the neutron-to-proton multiplicity ratio also shows a gradual evolution towards equalization, however, a full equilibration (mixing) is never achieved. The observed deviation from overall chemical equilibrium is very significant for the ^{112}Sn + ^{48}Ca reaction. The overall yields, energy spectra, and angular distributions predicted by Fermi-jet model calculations are not realistic. Predicted backward-angle jets are not observed in the experiment, while experimental multiplicities of non-equilibrium neutrons are significantly underestimated by the Fermi Jet model.

Contents

List of Figures x

List of Tables xviii

1 Introduction 1

2 Theory and Simulations 11
- 2.1 Introduction . . . 11
- 2.2 Nucleon Exchange Model . . . 12
- 2.3 Model for Statistical Decay of Excited Nuclei . . . 20
  - 2.3.1 Computer Code GEMINI for Statistical Decay . . . 21
  - 2.3.2 Moving Source Parameterization . . . 24
- 2.4 Non-equilibrium Particle Emission . . . 32
  - 2.4.1 Fermi-jet Model . . . 33

3 Experimental Setup 40
- 3.1 Introduction . . . 40
- 3.2 Mechanical Setup . . . 41
  - 3.2.1 Scattering Chamber and Target Ladder . . . 42
  - 3.2.2 PLF Detector Telescopes . . . 43
  - 3.2.3 LCP/IMF (ICDET) Detector Telescopes . . . 45
  - 3.2.4 Neutron Time-of-flight Spectrometer . . . 46
  - 3.2.5 Anti-coincidence Counters . . . 48
- 3.3 Electronic Setup . . . 49

4 Raw data, Calibrations & Analysis 64
- 4.1 Introduction . . . 64
- 4.2 Raw Data . . . 64
- 4.3 Calibrations . . . 71
  - 4.3.1 PLF Telescopes . . . 72
  - 4.3.2 ICDET Telescopes . . . 74
  - 4.3.3 Neutron Detectors . . . 75
- 4.4 Analysis . . . 82

5 **Results and Discussion** 89
- 5.1 Introduction 89
- 5.2 PLF Correlations 90
  - 5.2.1 PLF Energy-Angle Correlations 91
  - 5.2.2 Elastic Scattering and Reaction Cross Section 95
  - 5.2.3 PLF Energy-Charge Correlations 99
- 5.3 Energy and Angular Distributions of Sequentially and Promptly Emitted Particles 101
- 5.4 Fermi-jet Model Predictions for Prompt Particles 122

6 **Summary** 127

Bibliography 129

A **Fission Measurement and Simulations** 134
- A.1 Introduction 134
- A.2 Experimental Measurements 135
- A.3 Simulation Procedures 135
- A.4 Results 138

B **Pulse Shape Discriminator Module** 143
- B.1 Introduction 143
- B.2 Design of the Octal Dynode Pulse Handler Module DPH8 144
- B.3 Electronic Set-up 145

C **List of Abbreviations and Explanation of Terms** 148

List of Figures

1.1 Pictorial representation of a dissipative collision scenario. 2

2.1 Results of CLAT/NEM calculations for the impact parameter (b) dependencies of the interaction time (upper panel) and the total dissipated energy (lower panel), for the ^{112}Sn + ^{40}Ca (circles) and ^{112}Sn + ^{48}Ca (triangles) reactions at E/A=35MeV. 14

2.2 Results of CLAT/NEM calculations for the correlation between impact parameter (b) and deflection angle of the primary PLF (upper panel) for ^{112}Sn + ^{48}Ca at E/A=35MeV. The lower panel shows the differential cross section ($\frac{d\sigma}{d\theta}$) as a function of deflection angle (lower panel) extracted from the correlation shown in the upper panel. The grazing angle is indicated by the vertical lines at 4.2^o. 16

2.3 Correlation between the deflection angle of the primary PLF and total kinetic energy, as predicted by CLAT/NEM calculations for ^{112}Sn + ^{40}Ca (circles) and ^{112}Sn + ^{48}Ca (triangles) reactions at E/A=35MeV. 17

2.4 Results of the CLAT/NEM calculations for correlation between dissipated energy and mass-to-charge ratio of primary PLF (upper panel) and the ratio of the excitation energies of primary TLF and PLF (lower panel). Circles represent ^{112}Sn + ^{40}Ca reactions, while triangles represent ^{112}Sn + ^{48}Ca reactions, at E/A=35MeV. Horizontal lines correspond to either equal energy division (solid) or equal temperatures (dashed and dotted dashed). 18

2.5 Contour diagrams of the potential energy surfaces (PES) for fragmentation into PLF and TLF of the systems ^{112}Sn +^{40}Ca (upper panel), and ^{112}Sn + ^{48}Ca (lower panel), respectively. The energy contours are plotted vs neutron and atomic numbers of the PLF. Heavy solid lines originating from the "injection points" represent CLAT/NEM trajectory calculations [See text]. 19

2.6 Gemini predictions of neutron multiplicity for emission from PLF (left panel) and emission from TLF (right panel) vs. its excitation energy, for ^{112}Sn + ^{48}Ca. Various curves represent a different (primary) projectile- or target-like fragment prior to the evaporation process. 22

2.7 Gemini predictions of neutron-to-proton multiplicity ratio M_n/M_p for emission from PLFs (left panel) and emission from TLFs (right panel) vs. total excitation energy, for ^{112}Sn + ^{48}Ca. Curves represent M_n/M_p ratios calculated for emission from PLFs or TLFs with N/Z equal to that of the projectile or target (solid curves) or that of the composite systems (dashed curves). 24

2.8 Pictorial representation of the random emission pattern in velocity space from a moving emitter. Particles emitted with a given constant speed but into random directions, from a moving emitter outline a circular yield pattern in laboratory velocity space, centered at the velocity of the emitter with a radius equal to the speed of the particles in the rest frame of the emitter. 25

2.9 Similar to Fig. 2.8, showing a random emission pattern from two moving sources in velocity space. The velocities of two moving sources are represented by velocity vectors (the long and short one's) along with the velocity vector for the center-of-mass motion (intermediate length). 26

2.10 Plot of neutron energy spectra at three different laboratory angles. The two components, shown as dotted and dashed curves, correspond to emission from slow (target-like) and fast (projectile-like) moving sources shown in Fig. 2.9. Solid line represent the sum of two components. 28

2.11 Plot of galilei-invariant neutron yields vs. the neutron velocity components parallel and perpendicular to the beam direction, for two different energy losses. The continuous contour lines are obtained assuming sequential emission from PLFs and TLFs, the dotted contour lines represent an added contribution from hypothetical non-equilibrium source. 29

2.12 Typical plot of neutron energy spectra at three different laboratory angles. The dotted lines represent emission from the non-equilibrium source, the dashed-dotted lines represent emission from combined PLF and TLF (solid lines in Fig.2.10), while the solid line is the sum of all three contributions. 31

2.13 Pictorial view of the Fermi-jet emission mechanism. See text for details. 33

2.14 Fermi-jet inclusive energy spectra of neutrons for reaction ^{112}Sn + ^{40}Ca at E/A = 30, 35, and 50 MeV (left panel), and comparison of neutron and proton yield for ^{112}Sn + ^{40}Ca reaction at E/A=35MeV (right panel). 36

2.15 Fermi-jet angular distribution of neutrons (circles) and protons (triangles) from the reaction ^{112}Sn + ^{48}Ca at E/A = 30MeV. 37

2.16 Neutron-to-proton ratio of Fermi-jets versus particle energy for ^{112}Sn + ^{40}Ca (circles), and ^{112}Sn + ^{48}Ca (triangles) reactions at E/A = 30MeV. 38

2.17 Neutron-to-proton ratio of Fermi-jets versus laboratory angle for ^{112}Sn + ^{48}Ca (circles), and ^{112}Sn + ^{40}Ca (triangles) reactions at E/A = 30MeV. 39

3.1 Pictorial view of the experimental setup. 42

3.2 Pictorial view of the detectors inside reaction chamber. 43

3.3 Cross-sectional view of an LCP/IMF (ICDET) detector telescope. Also see ref. [FOX96] 45

3.4 Design of an Anti-coincidence Counter "Paddle" detector [adapted from LEO87]. 47

3.5 ^{22}Na light output spectra measured with one of the anti-coincidence counter "Paddle". The two shoulders visible corresponds to the 341-keV and 1.06-MeV "Compton edges" for the ^{22}Na γ-rays. 48

3.6 Block Diagram of the "trigger" logic. The electronics for each detector subsystem, represented as one particular block, is further described in the following figures. See Table 3.6 for abbreviations, terms and labels. 49
3.7 Electronic circuit diagram for telescopes PLF1 and PLF2 and Master Gate logic signal. See Table 3.6 for abbreviations, terms and labels. 51
3.8 Electronic circuit diagram for ICDET telescopes. See table 3.6 for abbreviations, terms and labels. 52
3.9 Electronic circuit diagram for neutron time-of-flight spectrometer. See table 3.6 for abbreviations, terms and labels. 54
3.10 Electronic circuit diagram for anti-coincidence "paddles". See. table 3.6 for abbreviations and labels. 56

4.1 Two-dimensional distribution (ΔE1-ΔE2) of the pulse-heights measured in first two elements of the telescope PLF1 for the reaction ^{112}Sn + ^{40}Ca at E/A=35MeV. 65
4.2 Two-dimensional distribution of pulse-heights measured at each end of the resistive chain in the position sensitive strip detector (the second element of a PLF telescope). 66
4.3 Two-dimensional distribution (ΔE-E) of pulse-heights measured in the Si (high-gain) and CsI elements of an ICDET detector telescope. 67
4.4 Two-dimensional distribution (ΔE-E) of pulse-heights measured in the Si (low gain) and CsI elements of an ICDET detector telescope. 68
4.5 Two-dimensional plot of total scintillation light output, Q_{tot}, of a neutron detector, vs. the partial light output, Q_{fast}, present in the leading part of the scintillator response. These two analog pulses are generated by the pulse-shape discriminator module(PSD) and digitized with a LeCroy-4300B FERA module. The upper panel is for Dynode 14, while the lower panel is for Dynode 11. The different response to neutrons (n) and γ-rays (γ) is illustrated by two branches of the light output correlation. 70
4.6 The measured light output of an anti-coincidence paddle placed in front of a neutron detector at 15° in the laboratory. 71
4.7 Two-dimensional distribution of the total energy vs. the energy measured in the first element (ΔE1) of a PLF telescope for the reaction ^{112}Sn + ^{48}Ca at 35MeV/A. 73
4.8 Two-dimensional distribution of pulse heights measured in second element (ΔE2) vs. the position on the face of a PLF telescope. 73
4.9 Dynode-14 light output spectra for each neutron detector, measured with a ^{22}Na γ-ray source. 76
4.10 Linear calibration for Dynode-14 light output with known positions of Compton edges, for each neutron detector. Calibration parameters, detector thresholds in equivalent electron and proton energies, along with error bars are also listed for each spectra. 77

4.11 A typical TOF spectrum (dotted curve) containing both neutrons and γ-rays, as obtained with a neutron detector at θ_{lab}=104°. The solid histogram represents events identified as neutrons by the neutron-γ pulse-shape discrimination circuitry. As indicated on the spectrum, the range of large times was used for determination of the background. 78

4.12 Detection efficiencies for neutron cells of various thickness, plotted versus the neutron energies, for a fixed threshold. 79

4.13 Assumed neutron energy spectra (symbols) with flat (upper panels) and Maxwellian (lower panels) distributions. Solid lines represent corresponding energy spectra after folding their time spectra with Gaussian distributions of 1 and 3 nsec FWHM. 80

4.14 Gamma-ray time-of-flight for different neutron detectors measured in coincidence with ^{252}Cf fission source. The FWHM (full width at half maximum), represents the time resolution of each neutron detector. 81

4.15 Energy spectra of Z=20 particles measured in a telescope (with strip detector) at forward angles for the reaction ^{112}Sn + ^{48}Ca at E/A=35MeV. Different strips shown here represent a different laboratory angle. The elastic yield was obtained from the energy spectra by fitting a Gaussian function. 83

4.16 Two-dimensional distribution of the charged yield measured in the PLF telescope at $< \Theta_{lab} > = 5.9^o$, plotted vs. atomic number (Z) and kinetic energy (E$_{lab}$). The upper panel is for the ^{112}Sn + ^{40}Ca reaction, while the lower panel represents the ^{112}Sn + ^{48}Ca reaction. Neutron and proton data were analyzed in coincidence with different conditions "gates" on the PLF kinetic energy, shown in the figure as gate1, gate2, gate3 and gate4. 85

4.17 Neutron time-of-flight spectra measured at different laboratory angles in coincidence with projectile like fragments (detected in PLF1 telescope) with energy between 1100-800 MeV in ^{112}Sn + ^{48}Ca reaction. Vertical lines in each spectra show a region of background determination, the horizontal lines represent the average background. 86

4.18 Energy spectra of neutrons from the ^{112}Sn + ^{48} Ca reaction for different laboratory angles. Data are represented by the symbols, while the curves represent a three moving-source fit. 87

5.1 Two-dimensional distribution of the observed charged-product yield, for the reactions ^{112}Sn + ^{48}Ca (upper left) and ^{197}Au+ ^{86}Kr (upper right) at E/A=35MeV, and for the reactions ^{209}Bi+ ^{136}Xe at E/A=28MeV (lower left) and E/A=55MeV (lower right), plotted vs. laboratory kinetic energy and deflection angle. 92

5.2 A pictorial representation of the reaction mechanism in scattering of argon from thorium at E/A=10MeV [WIL73]. This reaction exhibits a characteristic dissipative binary collision with orbiting type deflection function. 93

5.3 Analysis of the ridge line yield in Fig. 5.1 (upper panel, ^{209}Bi + ^{136}Xe at E/A=28MeV) in a representation of deflection angle versus measured average multiplicity of neutrons (upper panel) and light-charged particles with Z=1 (lower panel). The vertical bars illustrates FWHM values of the respective observed multiplicity distributions. Adapted from [BAL95b]. 93

5.4 Ratios of Elastic scattering yield to Rutherford scattering cross section plotted as functions of laboratory angles for the reactions ^{197}Au + ^{48}Ca (upper panel) and ^{112}Sn+ ^{48}Ca (lower panel) at E/A=35MeV. Curves represent calculations with the Fresnel diffraction model [FRA63, FRA71, FRA74] for different assumptions [see text]. 96

5.5 In the upper panel, the differential cross section ($\frac{d\sigma}{d\Omega}$) is plotted vs. the deflection angle for charged products detected in PLF telescope (upper panel), for quasi-elastic (circles) and highly dissipative (squares) ridges shown in the energy-angle correlations. In the lower panel, the differential cross section ($\frac{d\sigma}{d\theta}$) is plotted vs. the deflection angle. The circles represent data while triangles represent CLAT calculations. Solid, dashed, and dotted lines represent fits and interpolation for the data with assumptions discussed in text. 98

5.6 Two-dimensional distribution of the charged yield measured in the PLF telescope at $< \Theta_{lab} > = 5.9^o$, plotted vs atomic number (Z) and kinetic energy (E_{lab}). The upper panel is for the reaction ^{112}Sn + ^{40}Ca, while the lower panel represents the ^{112}Sn + ^{48}Ca reaction. The circles joined by lines, are quantitative model(NEM/EVAP) predictions for the E-Z correlations. Open circles represent calculations for representative primary reaction fragments predicted by the NEM. Solid circles represents calculations assuming the projectile as representative of the primary PLF. 102

5.7 Contour diagrams of the potential energy surfaces (PES) for fragmentation of the systems ^{112}Sn +^{40}Ca (upper panel), and ^{112}Sn + ^{48}Ca (lower panel), respectively, into PLF and TLF, for an angular momentum of ℓ=0 and a separation distance equal to the strong-absorption radius (R_{SA} = 12.06 and 12.3 fm, respectively). The energy contours are plotted vs neutron and atomic numbers of the PLF. Heavy curves represent pre-(solid) and post-(dashed) evaporation trajectory for PLFs. . 103

5.8 Energy spectra of neutrons from the ^{112}Sn + ^{48}Ca reaction at 35 MeV/A, measured at 15^o in coincidence with different gates on E-Z correlations, indicated in figure 4.16. Coincidence gates 1, 2, 3, and 4 in E-Z correlations are identified here as A,B,C, and D respectively. 104

5.9 Neutron energy spectra for different laboratory angles fitted with model of three moving sources for the reaction ^{112}Sn + ^{40}Ca at 35 MeV/A. Data are represented by the symbols. The solid curves represent a three-source fit, combining the contributions of neutrons from projectile-like (dotted curves), target-like (dot-dashed curves), and a hypothetical third source (dashed curves) moving with 55% of the beam velocity. 106

5.10 Neutron energy spectra for different laboratory angles fitted with model of three moving sources for the reaction ^{112}Sn + ^{48}Ca at 35 MeV/A. Data are represented by the symbols. The solid curves represent a three-source fit, combining the contributions of neutrons from projectile-like (dotted curves), target-like (dot-dashed curves), and a hypothetical third source (dashed curves) moving with 55% of the beam velocity. 107

5.11 Proton energy spectra for different laboratory angles fitted with model of three moving sources for the reaction ^{112}Sn + ^{40}Ca at 35 MeV/A. Data are represented by the symbols. The solid curves represent a three-source fit, combining the contributions of neutrons from projectile-like (dotted curves), target-like (dot-dashed curves), and a hypothetical third source (dashed curves) moving with 55% of the beam velocity. Φ represent the out-of-plane angle with respect to a plane defined by the PLF telescope and the neutron detectors. 109

5.12 Proton energy spectra for different laboratory angles fitted with model of three moving sources for the reaction ^{112}Sn + ^{48}Ca at 35 MeV/A. Data are represented by the symbols. The solid curves represent a three-source fit, combining the contributions of neutrons from projectile-like (dotted curves), target-like (dot-dashed curves), and a hypothetical third source (dashed curves) moving with 55% of the beam velocity. Φ represent the out-of-plane angle with respect to a plane defined by the PLF telescope and the neutron detectors. 110

5.13 The neutron multiplicity is plotted vs. the total excitation energy for the two systems ^{112}Sn + ^{40}Ca (dashed curves) and ^{112}Sn + ^{48}Ca (solid curves). In left panel, the neutron multiplicity for PLF (solid circles) and TLF (solid squares), is plotted as a function of total excitation energy, as obtained from fitting the different neutron components in the data. The total excitation energy is deduced from the velocity of the PLF by fitting a well defined PLF neutron component. In the right panel, the pre-equilibrium multiplicity (open squares) and the PLF+TLF (open circles) multiplicity are plotted as functions of the total excitation energy. 112

5.14 The neutron multiplicity for TLF neutron component (symbols in left panel), and PLF neutron components (symbols in right panel) for ^{40}Ca (solid circles) and ^{48}Ca (solid squares) induced reactions are plotted as a function of total excitation energy (bottom axis). Various curves represents the statistical model calculations (GEMINI). In left panel, the different curves represents statistical decay of ^{112}Sn, ^{111}Sn, ^{110}Sn, ^{111}In, ^{110}In, and ^{109}In. In right panel, the different curves for ^{48}Ca induced reactions, represents statistical decay of excited ^{48}Ca, ^{47}Ca, ^{46}Ca, ^{47}K, ^{46}K, and ^{45}K while for ^{40}Ca induced reactions, represents statistical decay of ^{40}Ca, ^{39}Ca, ^{38}Ca, ^{39}K, ^{38}K, and ^{37}K. Axis on the top represent the excitation energies of the primary fragments. 114

5.15 The ratio of TLF and PLF excitation energies is plotted vs. the total excitation energy for the reaction ^{112}Sn + ^{48}Ca. The data presented in this plot have been deduced from a comparison of the TLF neutron multiplicities with the evaporation calculations using the GEMINI code (see previous figure). The dashed curve represents prediction of the NEM calculations. 115

5.16 Shown in above figure is the comparison of neutron (circles) and proton (squares) energy spectra measured at an angle 20° w.r.t. the PLF. The left panels are for ^{40}Ca induced reactions while the right panels represents the ^{48}Ca induced reactions. The four panels (top to bottom as selected by gates in PLF kinetic energy), correspond to an increase in energy dissipation or a decrease in impact parameter. 117

5.17 The neutron-to-proton multiplicity ratio M_n/M_p for the PLF components vs. total excitation energy, for ^{112}Sn + ^{48}Ca (circles, left panel) and ^{112}Sn + ^{40}Ca (squares, right panel). Curves represent M_n/M_p ratios calculated for emission from projectile-like fragments with N/Z equal to that of the beams or the composite systems. 118

5.18 Shown in above figure is the comparison of neutron (circles) and proton (squares) energy spectra measured at an angle 60° w.r.t. the PLF. The left panels are for ^{40}Ca induced reactions while the right panels represents the ^{48}Ca induced reactions. The four panels (top to bottom as selected by gates in PLF kinetic energy), correspond to an increase in energy dissipation or a decrease in impact parameter. 120

5.19 The neutron-to-proton multiplicity ratio M_n/M_p for the non-equilibrium components vs. the total excitation energy, for ^{112}Sn + ^{48}Ca (circles) and ^{112}Sn + ^{40}Ca (squares) joined by lines. 121

5.20 Non-equilibrium component of neutron energy spectra (obtained after subtracting fitted PLF and TLF components) for different laboratory angles for the reaction ^{112}Sn + ^{48}Ca at 35 MeV/A. Data are represented by the symbols. The solid curves represent the Fermi-jet model predictions. 123

5.21 Pre-equilibrium neutron multiplicity is plotted vs. the total excitation energy. The solid symbols represent data for ^{48}Ca- (circle) and ^{40}Ca- (squares) induced reactions while the dashed and dashed-dotted curves represent results of the Fermi-jet model calculations for respective projectiles. 124

5.22 Neutron to proton multiplicity ratio for Fermi-jets, as predicted by the FERMI-JET model calculations for ^{48}Ca- (solid curves) and ^{40}Ca- (dashed curves) induced reactions on ^{112}Sn target as a function of total excitation energy. The ratio is plotted for each components, the forward-jets (circles) and the backward-jets (squares), predicted by the model. 125

A.1 Measured ^{252}Cf fission-fragment energy distribution. Solid curve is total fit with two Gaussian, while dotted curve represents the heavy-fragment component and dot-dashed curve represent the light-fragment component. 139

A.2 In the upper panel, the % yield of the fission fragments are plotted versus its mass. The symbols represents the data [adapted from BUD88], while solid line is the fit to the data with two Gaussian. In Lower panel, the yield of the fission fragments are plotted versus its velocity. The symbols represents the data [adapted from KIE92], while the solid line is the output of the simulation calculations with parameters from the fit in upper panel and an average mean relative velocity of 2.404cm/nsec between fission fragment. 140

A.3 a) The nuclear temparature, b) the average neutron multiplicity with solid line representing a theoretical prediction, c) the cascade neutron emission coefficient and d) the level density parameter are plotted versus the fission fragment mass. The data plotted in these figures [adapted from BUD88] were used in the simulation calculations. 141

A.4 Neutron energy spectra for different laboratory angles measured in coincidence with fission fragments from ^{252}Cf. Data are represented by symbols. The solid curve represents the results of Monte-Carlo simulation. 142

B.1 Typical scatter plot of the total charge, Q_{tot} versus the charge, Q_{fast}, of the leading portion of the signals produced by neutrons and γ-rays, respectively, in an NE213 scintillator detector. 144

B.2 Block diagram of the octal Dynode pulse handler module DPH8 (a) and electronic circuit diagram of an individual "PSD" adapted from [TÕK93]. Principle of operation of the circuit is discussed in [TÕK93]. 146

B.3 Photograph of the finished DPH8 module. 146

B.4 AutoCad rendering of the electronic set-up for a 16-detector neutron TOF spectrometer. 147

List of Tables

1.1 Reaction Parameters for the systems ^{112}Sn + ^{40,48}Ca at E/A=35MeV, as suggested by [WIL80] systematics. 10

3.1 Physical parameters of the PLF and MONITOR Detectors 57
3.2 Physical Parameters of the LCP/IMF (ICDET) Detector Telescopes. 58
3.3 Physical Parameters of the Neutron Detectors 59
3.4 Layout of the 3 CAMAC crates used in the present experiment. The glossary given in table 3.6 explains the abbreviations and terms used here for the various CAMAC modules. 60
3.5 Mapping of the 48 bits of pattern register (BITREG-1) to the different detectors and event trigger conditions. The glossary given in table 3.6 explains the abbreviations and terms used here for the various detectors and event types. 61
3.6 Glossary of abbreviations and terms used in electronic diagrams, i.e., Figs. 3.6-3.10 62

Chapter 1

Introduction

Beginning from the discovery of radioactivity (1896) and Rutherford's model of the atom (1911), until the recent discovery of the TOP quark (1994), we have acquired an in-depth understanding of the microscopic world of atoms and nuclei. The knowledge gained over a period of a century not only enabled us to explore the microscopic world but also helped us to understand the phenomena occurring on the cosmic scale, eg., evolution of universe and stars. Furthermore, the tools and techniques of nuclear science have found important applications in all fields of life including medicine, space research, power production, materials science, geology, and many more.

With the development of accelerators in the 1940's, it became possible to explore the fundamental properties of the nuclear forces and the structure of nuclei by bombarding a range of target nuclei with beams of light particles (electrons, neutrons, protons, deutrons, tritons, and alpha particles). The study of Coulomb excitation, elastic and in-elastic scattering, transfer reactions, and fission of heavy-nuclei provided information about the properties of the nucleus and its interactions. The phenomenology of heavy-ion collisions at low bombarding energies, i.e., from the interaction barrier to a few MeV per nucleon above the barrier, has been well studied in the past. It can be divided into four main categories (discussed below), depending on the range of impact parameters.

1. ELASTIC SCATTERING : For very large impact parameters and bombarding energies below the interaction barrier, only the long-range repulsive Coulomb force

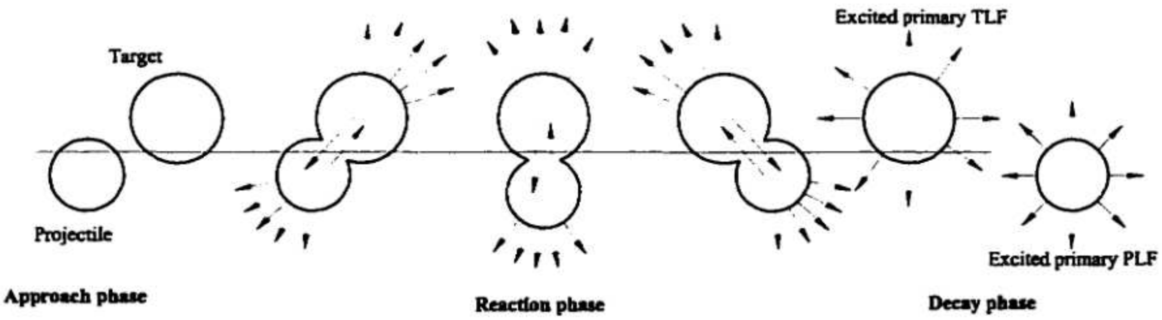

Figure 1.1: Pictorial representation of a dissipative collision scenario.

affects the trajectory of the incoming projectile and the scattering is purely elastic in nature, i.e., there is no exchange of particles or energy between the projectile and the target. The cross sections for elastic scattering can be described by the Rutherford scattering formula [RUTHE].

2. IN-ELASTIC SCATTERING / TRANSFER REACTIONS : For the range of impact parameters where the overlap of matter distribution of two nuclei is negligible and the short-range attractive nuclear forces are least effective, collisions result in the transfer of very few nucleons from the projectile to the target or vice-versa. Such reactions lead to product nuclei which are very similar to the reactants and have a very small or negligible excitation energy. Nuclear structure effects normally play a very important role in such collisions.

3. DISSIPATIVE COLLISIONS : Dissipative collisions occur in the range of impact parameters, where the two nuclei approach each other closely enough to overcome the repulsive Coulomb and centrifugal forces and where the attractive nuclear forces become effective. During the course of the collision, due to an overlap of target and projectile nuclear matter, a neck forms between the two reaction partners. Nucleons are exchanged between them, while the two reaction partners rotate about their common center of gravity for a fraction of a revolution. Due to the relative velocity of motion (v_{rel}), there is a mismatch between the momentum of a transferred nucleon and the average momenta of nucleons in the recipient nucleus. This mismatch is equilibrated by nucleonic collisions and eventually compensated by a change in total momentum of the recipient nucleus, thus resulting in a dissipation of kinetic energy. Subsequently, the repulsive forces drive apart the thermally excited reaction partners

(a.k.a. primary projectile- and target-like fragments), which can decay via different modes (sequential particle evaporation, fission, fragmentation, γ-ray emission, etc.) while proceeding along their Coulomb trajectories. These reactions can involve a significant amount of energy dissipation and a large number of transferred nucleons, however, the primary fragments remain largely similar to the reactants. A pictorial representation of a dissipative collision scenario is shown in Fig. 1.1

4. FUSION REACTIONS : For very small impact parameters, where nuclear forces completely overcome the repulsive Coulomb and centrifugal forces, fusion of the two interacting nuclei may lead to the formation of a compound nucleus. The compound nucleus, which is highly excited because of complete energy damping and complete transfer of nucleons can decay while moving along its trajectory.

The development of heavy-ion accelerators (late 70's) providing beams of particles with bombarding energies of several tens of MeV per nucleon, and the capability of accelerating almost any atomic nucleus, has opened a completely new regime for studying nuclear matter under extreme conditions of shape, spin, thermal excitation, and density. Nuclear systems formed in these conditions are predicted to show new phenomena such as multi-fragmentation (disassembly of the entire system into smaller clusters) or vaporization.

Over the past decade, considerable efforts have been made to explore the transitional features of heavy-ion collision dynamics developing from the well-known dissipative reaction mechanism at low bombarding energies [SCH84] (a few MeV per nucleon) to Fermi-bombarding energies (a few tens to 100 MeV per nucleon), where the relative velocity of the reaction partners are comparable to the nucleonic Fermi velocity (the average velocity of nucleons inside a nucleus, V_F=8.5 cm/nsec). It has been demonstrated [BAL95a, BAL95b, LOT92, QUE93, SCH92] that binary dissipative dynamics dominate the collision process in the bombarding energy range of up to several tens of MeV/nucleon. However, several new phenomena have also been discovered, such as neck fragmentation [LOT92, MON94, TÕK95a], dynamical emission of multiple intermediate-mass fragments [TÕK95b, TÕK96] (IMF), incomplete energy damping or saturation of dissipated energy [DJE96, LOT92, QUE93, XIA89], and the disassembly of a large fraction of the original projectile and target into small clusters and nucleons [PIA91].

In heavy-ion collisions, the distributions of various observables associated with massive reaction products, such as projectile-like and target-like fragments (PLF and TLF) are characteristic of the underlying reaction mechanism. For example, the correlations between emission angle of the projectile-like fragments (PLF) and dissipated energy, as well as the primary and secondary Z distributions of projectile-like fragments studied [BAL95a, BAL95b] for the reaction ^{209}Bi + ^{136}Xe at E/A=28MeV, have revealed the dominance of a dissipative reaction mechanism, similar to the one observed at lower bombarding energies [SCH84]. These correlations can also provide information about the strength of the attractive and repulsive components of the one-body mean field, the effectiveness of the frictional (dissipation) processes, and effect of the two-body nucleon-nucleon interactions on collision dynamics.

For a very heavy system, such as Bi + Xe, where the probability of forming a composite system (fusion) is very small, it has been shown [BAL95b] that most of the reaction cross section is exhausted by the dissipative reaction mode. For a medium-mass system, such as Sn + Ca, low-energy systematics [SCH86, WIL80], predict a significant cross section for fusion processes (1.2 b for fusion and 3.1 b for dissipative reaction). Due to a lack of experimental measurements for either reaction or fusion cross sections in the Fermi-energy domain, it is highly desirable to test the validity of predictions from low-energy systematics. Direct measurement of the projectile-like fragment (PLF) yield, over the entire angular range, allow us to extract the reaction cross section for dissipative collisions. In this work, the reaction cross section for ^{112}Sn + ^{48}Ca system is extracted in this manner.

In addition, the energy, mass, and charge distributions of massive PLF and TLF fragments is used to explore the transport phenomena. For example, the effect of the potential energy surface (driving-forces) in driving the system towards a chemical equilibrium, i.e., the equilibration of charge-to-mass asymmetry (mixing of nucleons) between target and projectile is considered in detail. There are several questions and answers which are still debatable and need, therefore, to be addressed by experimental measurements. For example, how does the equilibration of the charge-to-mass asymmetry depend on impact parameter or interaction time ? Is there a complete chemical equilibrium achieved in collisions at Fermi energies? Is the rate of equilibration is governed by the nucleon exchange process? Study of the relaxation of systems with large mass-to-charge asymmetry between target and projectile, as functions of impact parameter or interaction times, seems to provide the best tools to answer some of these questions.

The emission patterns of nucleons statistically evaporated from excited primary fragments carry important information about the reaction scenario, e.g., about the number of massive primary fragments, the total excitation energy and its division among the fragments. The angular distributions and yields of the statistically evaporated nucleons can be used for reconstruction of its emitter velocity and excitation energy. Once the excitation energy of each fragment is known, one can answer how this energy was shared among the fragments, whether the excitation energy was shared equally among the fragments or in proportion to their masses. In other words, one can conclude whether or not thermal equilibrium was achieved during the course of the collision ($E_i^* \propto A_i \tau_i^2$).

On the other hand, the yields of the particles sequentially evaporated from the excited target- and projectile-like fragments, when studied as functions of impact parameter, can provide information about the equilibration of the mass-to-charge density of the primary projectile and target, i.e., the degree of mixing of nucleons. In other words, one can study the evolution towards a chemical equilibrium of the target-projectile system during the course of the collision, an interesting transport phenomenon. As one can only measure directly the masses and charges of the post-evaporative projectile-like or target-like fragments during an experiment, some of the information about the primary-fragment mass-to-charge ratio is lost during the evaporation (decay) process. However, the yields of sequentially evaporated nucleons (neutrons and protons) are strongly correlated with the A/Z ratio of the primary fragments, providing a tool to probe the evolution of the A/Z (chemical) equilibration process.

For bombarding energies of a few MeV per nucleon and below, the particles emitted in damped nuclear reaction stem entirely from the decay of two fully equilibrated and accelerated projectile-like and target-like fragments. However, for bombarding energies of 5 MeV per nucleon and above, an additional particle emission mode has been observed. The particles emitted via this mode have relatively higher energies than the particles emitted sequentially from fully accelerated PLF and TLF. Such mode of particle emission, expected to set in during the early stages of the collision (during approach or interaction phase), has been known as pre-equilibrium, non-equilibrium, or prompt particle emission. Non-equilibrium particle emission processes have been studied experimentally [DEM70, HIL87, HOL63, HOL83, HOL86, SCH84, VER69, WOO65] to some extent for heavy-ion induced fusion and fusion-like reactions. The existence of such processes has also been established [PET89, WIL89b] for ^{40}Ar- and ^{58}Ni-induced damped reactions at bombarding energies between 10 and 16 MeV/u. However, information on non-equilibrium particle emission in dissipative reactions is still very scant [HIL88, PET89, REM88, WIL87, WIL89a, WIL89b, WIL89c] and limited to relatively low bombarding energies.

In light of the discovery of incomplete energy damping [DJE96, LOT92, QUE93] at Fermi-bombarding energies, i.e., only a fraction (50-60%) of the relative kinetic energy of motion is dissipated into thermal excitation of projectile- and target-like fragments, it becomes important to understand the role of non-equilibrium particles in the balance of dissipated energy, ie., the amount of energy and momentum carried away by the non-equilibrium particles. An increase in multiplicity of non-equilibrium particles is expected with increasing bombarding energy [WIL89b], thus reducing the amount of energy available for excitation of the interacting nuclei. From the measured emission probabilities and energy spectra of energetic non-equilibrium particles, one can quantitatively estimate the amount of energy carried away by non-equilibrium particles. Also, the effect of non-equilibrium particle emission is of importance for the prospects of forming nuclear systems at critically high temperatures.

In addition, the mechanism responsible for the emission of non-equilibrium energetic particles during the heavy-ion collision process is not well understood. Several non-equilibrium models [BLA85, BON79, BON80, RAN87, REM88] have been developed and applied with varying success [BLA85, HIL88, MAC85, REM88, WIL87, WIL89a, WIL89b] to describe non-equilibrium emission processes for either light-ion induced collisions or heavy-ion reactions at relatively low bombarding energies. In these models, a nucleon transferred between reaction partners in the fast approach phase initiates a non-equilibrium cascade in the receptor nucleus, where emission is possible from any stage of the equilibration process. A particular and very interesting mode of fast-particle emission is predicted within the currently most popular reaction models, which are based on a dominance of mean-field effects, such as in NEM [SCH86], BUU [UEH33] and other one-body approaches. In these coherent "Fermi-jet" modes [AIC85, AIC86, BON79, BON80, CAS87, DAV84, LER85, MÖH85, RAN87, RAN93, REM84, ROB79], the addition of the Fermi velocity of a transferred nucleon and the relative nucleus-nucleus velocity may lead to an energy of the nucleon that leaves it unbound in the receptor nucleus. Such nucleons can then be emitted in a forward or backward jet, depending on whether they originate in the projectile or the target, respectively. With the moderate success of the Nucleon Exchange Model [SCH86] in qualitatively describing the collision dynamics at Fermi bombarding energies, it becomes interesting and crucial to test the predictions of the Fermi-jet model [BON79, BON80, RAN87, RAN93], which is a consequence of the one-body nucleon exchange process.

In the present work, a systematic study has been performed for ^{112}Sn + ^{48,40}Ca reactions at E/A = 35MeV. The emission probabilities and patterns of light particles (neutrons and protons), detected in coincidence with projectile-like fragments, have been used as tools to probe transport phenomena in the Fermi-energy domain. Furthermore, the correlations between deflection angle of the projectile-like fragments (PLF) and its dissipated energy, reaction yields, and the post-evaporation Z-distributions, which are also prime indicators of transport phenomena, have been studied to understand the overall dynamics of the collisions at Fermi energies. In addition, the mechanism responsible for emission of non-equilibrium particles and their role in limiting energy dissipation is explored.

In order to optimize the sensitivity of the experiment, in which both neutrons and charged particles are measured, the medium-weight systems ^{112}Sn + ^{48,40}Ca were chosen as a compromise. ^{40}Ca and ^{48}Ca projectiles were chosen for comparison, since they provide for the largest difference in N/Z value available for stable medium-weight projectile isotopes. The PLF distributions from these two reactions are of considerable interest also, because they are affected to a different extent by the underlying potential energy surface and the subsequent evaporation processes. Of particular interest are the evolution of N/Z of the primary projectile-like fragments with increasing energy dissipation, and the extent to which yields of the non-equilibrium particles are affected by the N/Z of the beam. For the ^{40}Ca and ^{48}Ca projectiles, these ratios are N/Z=1.0 and 1.4, respectively, while N/Z=1.24 for the target, ^{112}Sn. The N/Z ratios for the composite systems for two cases are N/Z=1.17 and 1.28, respectively. Parameters pertinent to the reactions are collected in Table 1.1 for a bombarding energy of E/A=35MeV.

Chapter 2 discusses the theoretical models employed for the interpretation of experimental results. The underlying physical assumptions, sensitivities, and predictive power of the Nucleon Exchange based Classical Trajectory Model (CLAT), the Statistical Decay Model (GEMINI), the "Moving-Source" Model, and the Fermi-jet Model (FJET) for promptly emitted particles (also called Fermi-jets), are discussed in detail. A subsection of Chapter 2 has been devoted to the results of simulation calculations performed with the "Moving Source Model" prior to the experiments. These simulation calculations have aided the design and planning phase of the experiment. A similar model was also used for extracting various physical quantities during the analysis of the experimental data.

In Chapter 3, details of the experimental setup are presented. It includes the mechanical setup, the types of detector systems used for measurement of the reaction products, and the electronic setup used for processing the analog signals from each detector system. The conditions which triggered the acquisition of data and the structure in which data were stored for off-line analysis are also discussed in this chapter.

The first section of Chapter 4 describes the on-line performance of different detector systems. One- and two-dimensional graphic representations are employed for presentation of raw data, followed by a section on the methods used for the calibration of each detector system. The last section of Chapter 4 describes the analysis procedures adopted for extracting various physical observables.

Final results are discussed in Chapter 5. Conclusion are deduced on the basis of characteristic correlations between various experimental observables and their comparison with suitable model and simulation calculations. A summary of the key findings is presented in Chapter 6.

A Bibliography of the referred work is collected at the end of this document, followed by three appendices. Appendix A discusses the energy and angular distribution of neutrons measured from spontaneous fission of ^{252}Cf, a process used to assess the performance of the multi-detector neutron spectrometer. Simulation calculations also provided a consistency check for the detector efficiency corrections predicted by Cecil et al. [CEC79]. Appendix B discusses the details of an electronic pulse-shape discriminator module (Dynode pulse handler, DPH8), which was designed and developed for seperation of neutrons from γ-rays, based on their characteristic pulse shape detected by liquid-scintillator detectors. Abbreviations and terms used in this document are explained in Appendix C.

Table 1.1: Reaction Parameters for the systems ^{112}Sn + ^{40,48}Ca at E/A=35MeV, as suggested by [WIL80] systematics.

	^{112}Sn + ^{40}Ca	^{112}Sn + ^{48}Ca	
E / A	35.0	35.0	MeV
E_{cm}	1032	1178	MeV
$(E_{cm}-V_c)/\mu$	31.97	31.52	MeV/nucleon
ι_{max}	433	507	ħ
σ_R	4.1	4.3	b
σ_{fus}	0.2	0.2	b
θ_{graz}	5.2	4.2	deg
T_{max}	7.1	7.4	MeV
μ	29.47	33.6	amu
$(N/Z)_P$	1.00	1.40	–
$(N/Z)_T$	1.24	1.24	–
$(N/Z)_{P+T}$	1.17	1.28	–
R_{int}	12.06	12.30	fm
$V_c(R_{int})$	119.2	116.9	MeV
TKE_{min}	121	119	MeV
ι_{RLDM}	70	78	ħ

Chapter 2

Theory and Simulations

2.1 Introduction

This chapter presents a theoretical description of the models and simulation calculations, which were employed for interpretation of the experimental data. Section 2.2 presents a conceptual description of the Nucleon Exchange Model [RAN78, RAN79, RAN82], the assumptions used by the model, and its success in quantitatively describing experimental observables at bombarding energy of a few MeV per nucleon. Some of the model predictions for the ^{112}Sn + ^{48,40}Ca systems at E/A=35MeV are also discussed. Section 2.3 discusses the concepts of Statistical Decay of excited nuclei. In Subsection 2.3.1, the predictions of the computer code GEMINI [CHA88a, CHA88b], which is a Monte Carlo implementation of the Statistical Decay model, are discussed for correlations which are directly affected by the transport phenomena. For example, the ratios of evaporated neutron-to-proton multiplicities as functions of dissipated energies. Subsection 2.3.2 presents a discussion of a schematic moving-source model, which is based on the statistical emission of particles from an excited nuclei. In the last section (2.4), phenomena of the prompt or non-equilibrium particle emission are discussed, in particular the Fermi-jet model [BON79, BON80, RAN87, RAN93] predictions for emission of fast-particles (jets), which are of relevance to the study of critically hot nuclear systems [see Chapter 1]. The predictions of all the models and simulation calculations discussed in this chapter are compared with the experimental results in Chapter 5.

2.2 Nucleon Exchange Model

The Nucleon Exchange Model (NEM) has been quite successful in quantitative reproduction of experimental results for heavy-ion collisions at low bombarding energies (few MeV/A). At Fermi energies, it has also been successful in describing overall qualitative features of the reaction mechanism. However, the quantitative reproduction of data is not very good. Other processes, not considered in this model, such as, intermediate-mass fragment emission, non-equilibrium particle emission, and the complete disassembly of the projectile-target system, start to play an important role in the dynamics of the collision.

In the NEM model, which was developed by Randrup and collaborators [DOS85, RAN78] during the collision process, the projectile and target nuclei approach one another and form a dinuclear system which rotates about the center of mass. The balance of Coulomb, centrifugal, and nuclear forces determines the extent of penetration of two nuclei into each other's matter distribution. A "window" or "neck" forms in the overlap region of the matter distributions, through which nucleons can freely transfer from projectile to target or vice-versa. Due to the relative velocity of motion (v_{rel}), the mismatch between the momentum of a transferred nucleon and the average momenta of nucleons in the recipient nucleus is compensated by a change in total momentum of the recipient nucleus, resulting in a dissipation of kinetic energy. The exchange process is assumed to be fast on the time scale of the collision, and that the excess energy of the transferred nucleon is immediately thermalized after the transfer (adiabaticity). The system rotates by a fraction of a revolution, while kinetic energy and angular momentum are dissipated. Eventually, the dinuclear system re-separates into two massive projectile-like (PLF) and target-like (TLF) thermally excited fragments, due to the repulsive Coulomb and centrifugal forces, and quickly accelerate to their asymptotic velocities. In this model, the trajectory of dinuclear system is determined by conservative Coulomb (long-range) and nuclear (short-range or proximity) forces and a non-conservative or dissipative friction-like force resulting from exchange of nucleons.

In the NEM, macroscopic observables are integrated along multi-dimensional system trajectories with the initial conditions given by impact parameter (b), velocity of relative motion (v_{rel}), nuclear mass (A) and charge (Z) of the projectile and the target. For each impact parameter, the model calculates the average energy loss, deflection angle, and spins of the primary fragments, as well as the averages and variances of the fragment A, Z, and excitation energy. According to NEM, at Fermi energies, the excitation energy of the primary fragments accounts for almost the entire energy loss, E_{loss}. The division of the total excitation energy between projectile-like and target-like fragments, E^*_{PLF}/E^*_{TLF}, reflects properties of excitation and relaxation mechanism.

In the NEM, all transport phenomena, including the dissipation and equilibration of relative kinetic energy, arise from the exchange of independent nucleons. The excitation energy deposited in the recipient nucleus (2) by the transfer of a single nucleon from donor nucleus (1) is given approximately by

$$\omega^{(2)}_{12} = \epsilon_{F1} - \epsilon_{F2} - \vec{\mathbf{p}} \cdot \vec{\mathbf{u}} = F_{12} - \vec{\mathbf{p}} \cdot \vec{\mathbf{u}} \tag{2.1}$$

where ϵ_{F1} and ϵ_{F2} are the Fermi energies of the donor and recipient nuclei, respectively, $\vec{\mathbf{p}}$ is the Fermi momentum vector of the transferred nucleon, and $\vec{\mathbf{u}}$ is the relative velocity vector of the two nuclei. The quantity F_{12}, substituted for $\epsilon_{F1} - \epsilon_{F2}$, in Equation 2.1, is referred to as the static driving force for nucleon exchange. The excitation energy deposited in the donor nucleus is given by,

$$\omega^{(1)}_{12} = \epsilon_{F1} - \frac{p^2}{2m} \tag{2.2}$$

where m is the mass of the transferred nucleon. The recipient nucleus receives the major fraction of the total excitation energy generated in the exchange. However, since there is a free exchange of nucleon in both directions, this effect is averaged out. In addition, due to Pauli blocking, a nucleon can only be transferred, if there is an unoccupied state in the recipient nucleus. As a result the nucleon exchange process drives the dinuclear system toward thermal equilibrium. The excitation energies of the two interacting nuclei is taken out of the relative motion, a transfer process that

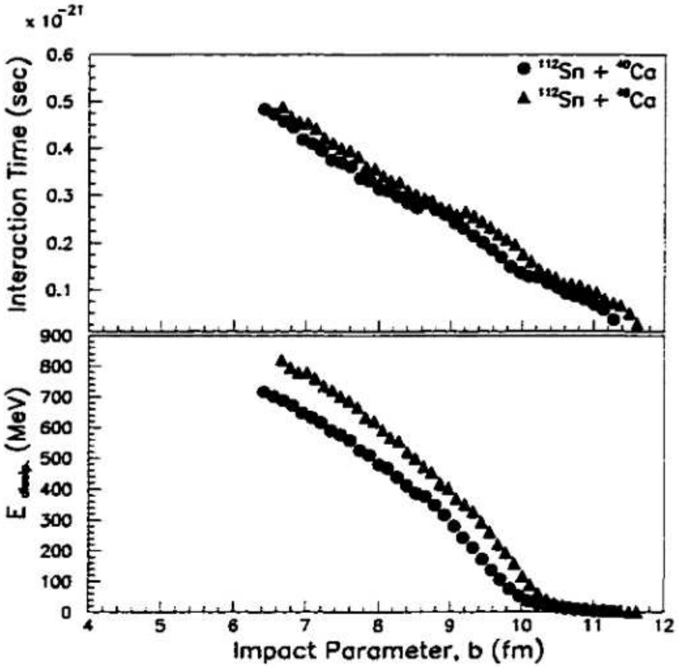

Figure 2.1: Results of CLAT/NEM calculations for the impact parameter (b) dependencies of the interaction time (upper panel) and the total dissipated energy (lower panel), for the ^{112}Sn + ^{40}Ca (circles) and ^{112}Sn + ^{48}Ca (triangles) reactions at E/A=35MeV.

is described in terms of classical friction forces. The time evolution of the average macroscopic observables is described in terms of Lagrange-Rayleigh equations of motion as described in detail elsewhere [DOS85, RAN78, RAN79, RAN82]. Calculations were performed for the ^{112}Sn + ^{48,40}Ca systems at E/A=35MeV with a computer code CLAT (Classical Trajectory Calculations) [SCH86], which is an implementation of the NEM model discussed above, with a liquid-drop model interaction potential modified for proximity effects (adiabatic limit) for the nuclear interaction. The results of these CLAT/NEM calculations are collected in Figs. 2.1-2.2 and discussed further below.

Shown in Fig. 2.1 are results of CLAT/NEM calculations for the impact parameter (b) dependencies of the interaction time (upper panel) and the total dissipated energy (lower panel), for the ^{112}Sn + ^{40}Ca (circles) and ^{112}Sn + ^{48}Ca (triangles) reactions at E/A=35MeV. One observes almost linear correlation between the impact parameters and the interaction times for both systems, except for a very small offset, which is due to the different sizes of the projectiles, ($R \approx R_0 \cdot A^{1/3}$ fm, where $R_0 \approx 1.2$ fm) with $R_{^{48}Ca} \approx 4.38$ fm, and $R_{^{40}Ca} \approx 4.10$ fm. Once projectile and target nuclei form a dinuclear system, which survives for times of the order of 10^{-22} to 10^{-21} seconds, the kinetic energy of relative motion is dissipated due to exchange of nucleons. As explained previously, this dissipation is effected by the exchange of independent nucleons, until the dinuclear system re-separates as PLF and TLF. With decreasing impact parameter. the overlap region of the matter distributions increases. Since this region defines the size of the "neck" through which nucleons can freely transfer from projectile to target or vice-versa, lead decreasing impact parameter to higher degrees of energy dissipation. For a certain range of relatively small impact parameters, the model predicts fusion of the target-projectile system.

From Fig. 2.1, one also notices that, for a given value of impact parameter (say b = 8 fm), more energy is dissipated in the case of ^{112}Sn + ^{48}Ca system than for the ^{112}Sn + ^{40}Ca system. This difference arises from two reasons. The first effect is due the size of the projectile, which defines the size of the overlap region. The second effect is caused by different mean currents of nucleons transfered from one nucleus to the other in a short time interval. The average numbers of neutrons, $\Delta\nu_N$, and protons, $\Delta\nu_P$, which "attempt" a transfer during a given short time interval Δt can be described as

$$\Delta\nu_N = N_N \Delta t \approx \frac{N}{A} n_0 \pi c_{eff}^2, \qquad \Delta\nu_Z = N_Z \Delta t \approx \frac{Z}{A} n_0 \pi c_{eff}^2, \tag{2.3}$$

where N and Z refer to the neutron and proton number of the combined dinuclear system, $n_0 = 0.263$ fm$^{-2}10^{22}$s^{-1} is the standard one-way flux in nuclear matter, and $\sigma_{eff} = \pi c_{eff}^2$ is the effective neck radius. The ^{112}Sn + ^{48}Ca system has relatively higher mean current of neutrons ($\Delta\nu_N$), because of larger N/A ratio with respect to ^{112}Sn + ^{40}Ca system, leading to relatively higher energy dissipation.

Shown in the upper panel of Fig. 2.2 are results of NEM calculations for the correlation between impact parameter (b), and deflection angle (Θ_{lab}) of the scattered primary PLF for ^{112}Sn + ^{48}Ca reactions at E/A=35MeV. After fitting the correlation between impact parameter and deflection angle with a smooth functional form, the differential cross section as a function of deflection angle was calculated using the relation $\frac{d\sigma}{d\Theta_{Lab}} = 2\pi b \cdot (\frac{db}{d\Theta_{Lab}})$. This differential cross section is plotted in the lower panel of Fig. 2.2 as a function of deflection angle. The total cross section for the dissipative reaction yield, as predicted by the NEM calculations, and obtained by

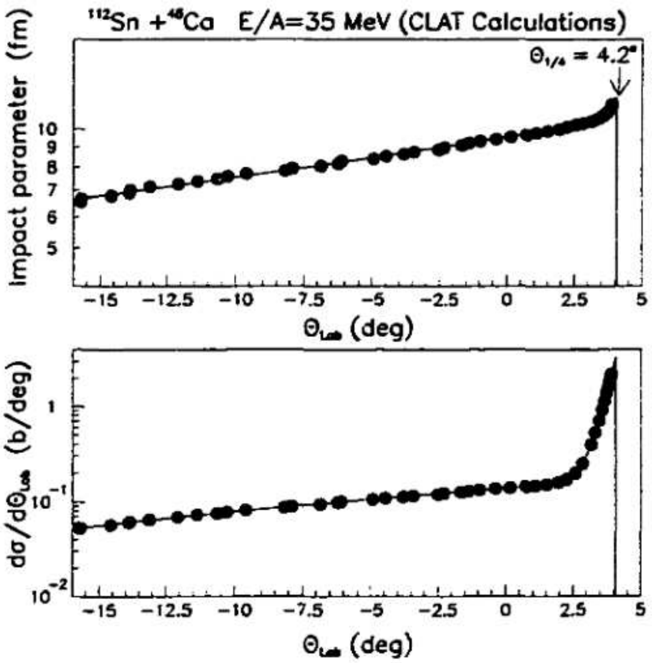

Figure 2.2: Results of CLAT/NEM calculations for the correlation between impact parameter (b) and deflection angle of the primary PLF (upper panel) for ^{112}Sn + ^{48}Ca at E/A=35MeV. The lower panel shows the differential cross section ($\frac{d\sigma}{d\theta}$) as a function of deflection angle (lower panel) extracted from the correlation shown in the upper panel. The grazing angle is indicated by the vertical lines at 4.2°.

integrating the differential cross section over the entire angular range yielded a value of (3.0±0.1) b. In addition to this cross section, the NEM predicts a significant cross section of 1.3 b for fusion of ^{112}Sn + ^{48}Ca system. In Chapter 5, experimental results are compared to these model calculations.

Shown in Fig. 2.3 is the correlation between the deflection angle of the primary PLF and the total kinetic energy, as predicted by NEM/CLAT calculations for ^{112}Sn + ^{40}Ca (circle) and ^{112}Sn + ^{48}Ca (triangles) systems. It is seen that the total kinetic energy of the system decreases in a correlated fashion with deflection angle of the primary PLF. This decrease in total kinetic energy is a direct consequence of the dissipation mechanism, which takes energy from relative motion and transforms it into thermal excitation of the system, while the dinuclear system rotates. An orbiting behavior is clearly visible from the dependence of the PLF deflection angle on final kinetic energy. For large energy losses, a negative angle scattering results in the model calculations. The overall interaction time increases scattering to more and more negative angles, of course, this process leads to highly excited and, therefore, unstable primary fragments. The decay of the excited projectile-like and target-like

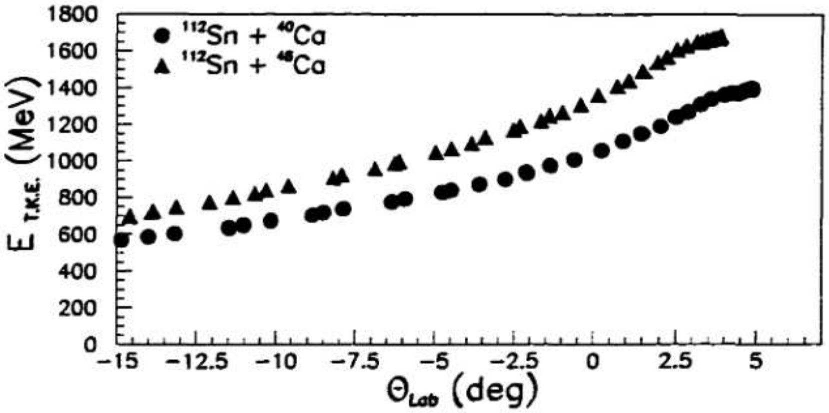

Figure 2.3: Correlation between the deflection angle of the primary PLF and total kinetic energy, as predicted by CLAT/NEM calculations for ^{112}Sn + ^{40}Ca (circles) and ^{112}Sn + ^{48}Ca (triangles) reactions at E/A=35MeV.

fragments was modeled with a statistical (decay) evaporation model, which will be discussed in the following section. In Chapter 5, the angular distributions of the secondary fragments produced at the end of decay process are shown and discussed in the context of experimental PLF angular distributions.

Fig. 2.4 shows the results of the CLAT/NEM calculations for correlations between dissipated energy and mass-to-charge ratio of primary PLF (upper panel) and the ratio of the excitation energies of primary PLF and TLF (lower panel). Circles show results obtained for ^{112}Sn + ^{40}Ca while triangles represent ^{112}Sn + ^{48}Ca. Horizontal lines correspond to either equal energy division (solid) or equal temperatures (dashed and dotted dashed) of PLF and TLF. The trend in the evolution of the N/Z ratio of the primary PLF fragments with excitation energy are very different for the two reactions. For ^{112}Sn + ^{40}Ca (circles), the average N/Z value of the primary PLFs increases with increasing excitation energy, while for ^{112}Sn + ^{48}Ca system (triangles) the average N/Z value of the primary PLFs decrease. In both cases, the evolution of the average N/Z of the primary PLF is towards the overall N/Z of the composite system. However, this evolution is very gradual and governed by the slow progress of the nucleon exchange processes with time. This effect is attributed to relatively small driving forces for nucleon transfer and short interaction times. Calculation for the potential energy surface for binary divisions of the two systems into PLF and TLF pairs are shown in the following figure. In addition, as seen in the lower panel of Fig. 2.4, the sharing of total excitation energy between primary PLF and TLF is not charac-

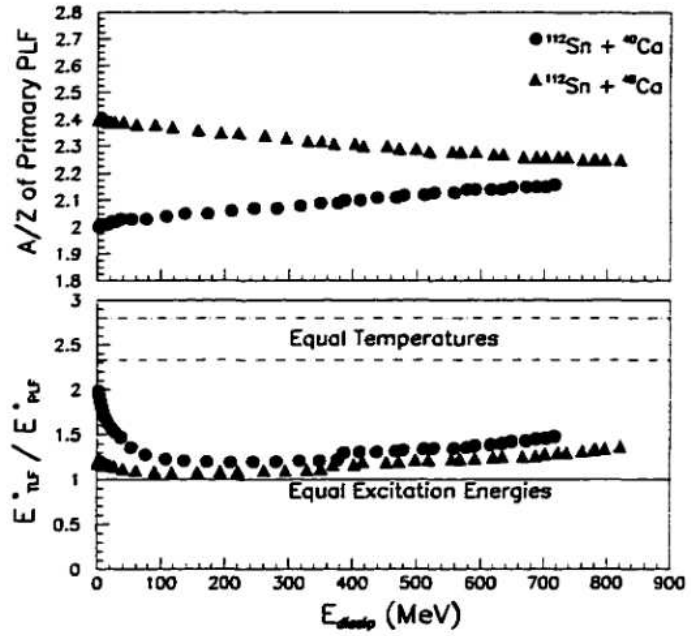

Figure 2.4: Results of the CLAT/NEM calculations for correlation between dissipated energy and mass-to-charge ratio of primary PLF (upper panel) and the ratio of the excitation energies of primary TLF and PLF (lower panel). Circles represent ^{112}Sn + ^{40}Ca reactions, while triangles represent ^{112}Sn + ^{48}Ca reactions, at E/A=35MeV. Horizontal lines correspond to either equal energy division (solid) or equal temperatures (dashed and dotted dashed).

teristic of thermal equilibrium. In both cases, target-like and projectile-like fragments receive comparable excitation energies. Typically, the TLF receives a little more excitation energy than the PLF, for the entire range of impact parameters (peripheral to central collisions). For very low excitation energy, once observes large difference in the energy division between projectile and target for ^{112}Sn + ^{40}Ca system. For very peripheral collisions, the two nuclei are always close to their ground states, i.e., both have approximately the same, zero temperature. As soon as nucleon exchange becomes important in a collision, the projectile target system is driven away from thermal equilibrium. Subsequent exchange processes act as a feed back mechanism and tend to equalize different temperatures of the interacting fragments.

Fig. 2.5 shows contour diagrams of the potential energy surfaces (PES) for fragmentation into PLF and TLF of the systems ^{112}Sn +^{40}Ca (upper panel), and ^{112}Sn + ^{48}Ca (lower panel), respectively, for an orbital angular momentum of ℓ=0 (b=0) and a separation distance equal to the strong-absorption radius (R_{SA} = 12.06 and 12.3 fm, respectively). The energy contours are plotted vs. neutron and atomic numbers of the PLF. Effects of closed nuclear shells for N or Z = 20, and N = 28 are included

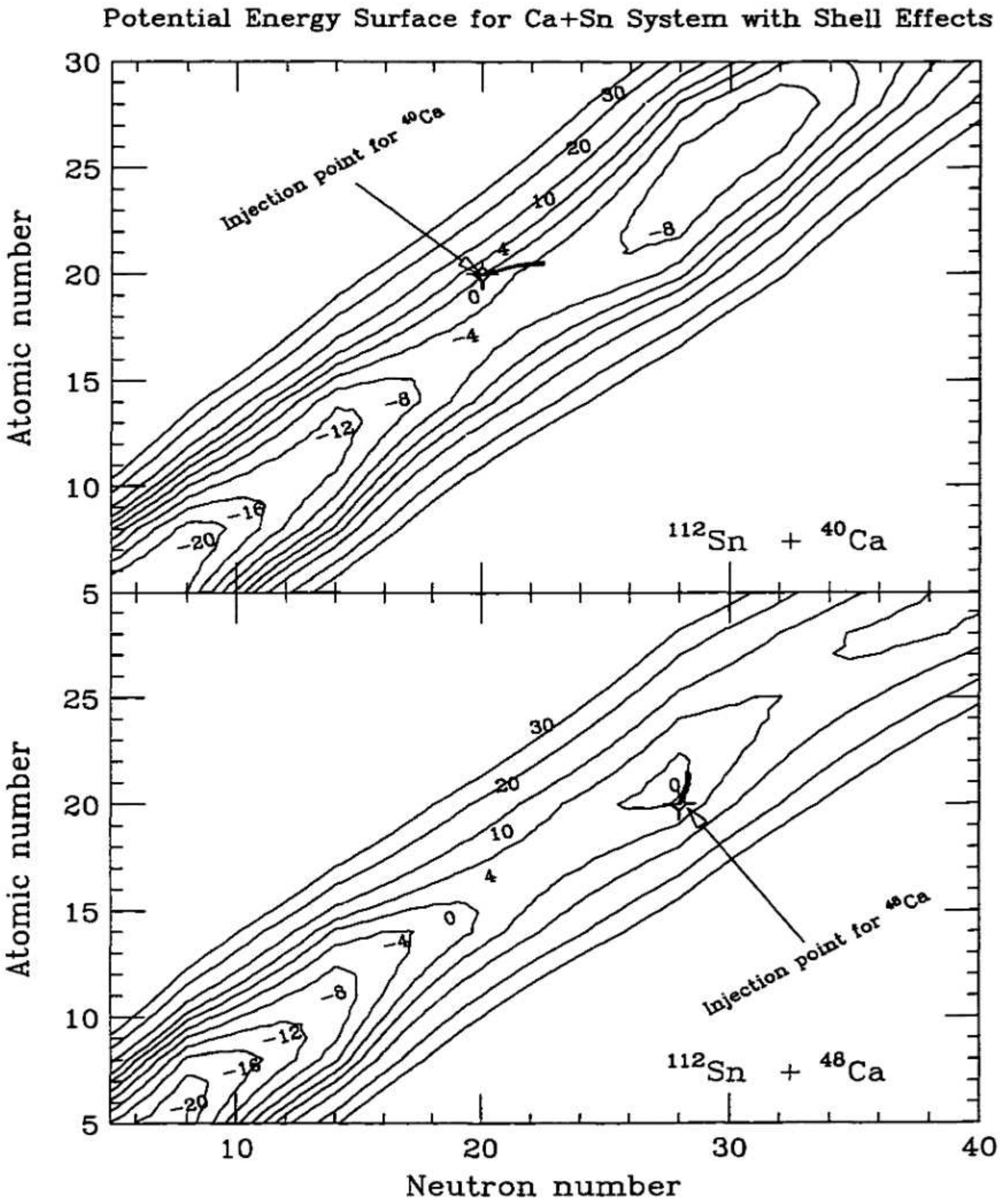

Figure 2.5: Contour diagrams of the potential energy surfaces (PES) for fragmentation into PLF and TLF of the systems ^{112}Sn +^{40}Ca (upper panel), and ^{112}Sn + ^{48}Ca (lower panel), respectively. The energy contours are plotted vs neutron and atomic numbers of the PLF. Heavy solid lines originating from the "injection points" represent CLAT/NEM trajectory calculations [See text].

in the calculations. The CLAT/NEM trajectory calculations for the primary PLF are shown as heavy solid lines originating from the "injection points" (projectile-target combination) in each plot.

Comparing the upper with the lower panel of Fig. 2.5, one notices that, near the "injection points", the slope of the PES for the ^{112}Sn + ^{40}Ca system is steeper than and directed to opposite that for the ^{112}Sn + ^{48}Ca system. For the ^{40}Ca-induced reaction, the surface shows a steep gradient towards larger PLF-N/Z values. On the other hand, the "injection point" for the reaction ^{112}Sn+^{48}Ca is already located near the local minimum of the potential energy surface. Quantitatively, the CLAT/NEM calculations, represented in Fig. 2.5 by the heavy solid lines originating from the injection points, predict the primary PLF to gain neutrons in case of the ^{112}Sn + ^{40}Ca system. On the other hand, for ^{112}Sn+^{48}Ca system, the primary PLF is expected to gain protons during the course of the collision. Here, one clearly sees the effect of the potential surface energy in driving the system towards equilibrium. The effects of a secondary decay of the excited primary PLFs were also studied. They are discussed in detail in Chapter 5.

2.3 Model for Statistical Decay of Excited Nuclei

The decay properties of the excited nuclei produced in heavy-ion collisions have been successfully described by statistical model calculations [GAV80, NIC80, PUH77]. In such a model, a thermally excited and statistically equilibrated nucleus can decay to the ground state by emitting neutrons, protons, α-particles, γ-rays, and heavier fragments, and or by fission. The decay, which is purely statistical in nature, is governed by the number of available nuclear configurations (modes) and the respective probabilities for decay to each configuration. A parent nucleus with a given excitation energy and angular momentum, during decay may populate daughter nuclei in a range of masses, charges, and final excitation energies, with different decay probabilities for each daughter channel. Each daughter, in turn, becomes the parent for the next decay step, and the process continues until there is no excitation energy or angular momentum left.

Most of the present-day statistical model calculations are based on the Hauser-Feshbach formalism [HAU52], which gives the cross section for a given reaction to proceed from entrance channel A to exit channel B, while conserving the angular momenta and parity.

$$\sigma_{A\rightarrow B} = \sum_{J} \frac{2J+1}{(2I_p+1)(2I_t+1)} \cdot \sum_{s,l} T_l(A) \cdot \frac{\sum_{s,l} T_{l'}(B)}{\sum_{s'',l''} T_{l''}(B')} \tag{2.4}$$

where T_l represent the transmission coefficients for compound nucleus formation in channel A and subsequent decay in channel B, with compound nucleus spin J resulting the coupling of target and projectile spins, I_t and I_p, respectively, to the orbital angular momentum l.

Statistical-model calculations have been implemented in computer codes using either a multi-step grid method (CASCADE)[PUH77] or a multi-step Monte-Carlo [CHA88, GAV80, NIC80] method. In case of the multi-step grid method, angular momentum and excitation energy of each parent nucleus defines a two-dimensional coordinate grid. For each of the bins in this coordinate grid, the respective probabilities for each mode of decay are calculated leading to various bins in the respective grid for the daughter nuclei. The cross sections are then redistributed according to initial postulations and decay probabilities throughout the calculations, as the daughter in turn becomes the parents in the next decay step. However, in case of the Monte-Carlo method, all decay modes are sampled according to the decay probabilities for different daughter channels, generating a sample of individual decay chains. In the latter case, calculations conserve correlations between various quantities, such as particle yields and their angular distributions, which are typically not available in the former case.

2.3.1 Computer Code GEMINI for Statistical Decay

Initially, most of the statistical computer codes were developed for fusion studies, where experimental excitation energies were $\leq$200 MeV. These codes were inadequate to treat nuclei with large excitation energy and angular momentum encountered in heavy-ion collisions at Fermi-energies. Also, the emission of intermediate-mass fragments, which becomes an important mode of decay for large excitation energies, was

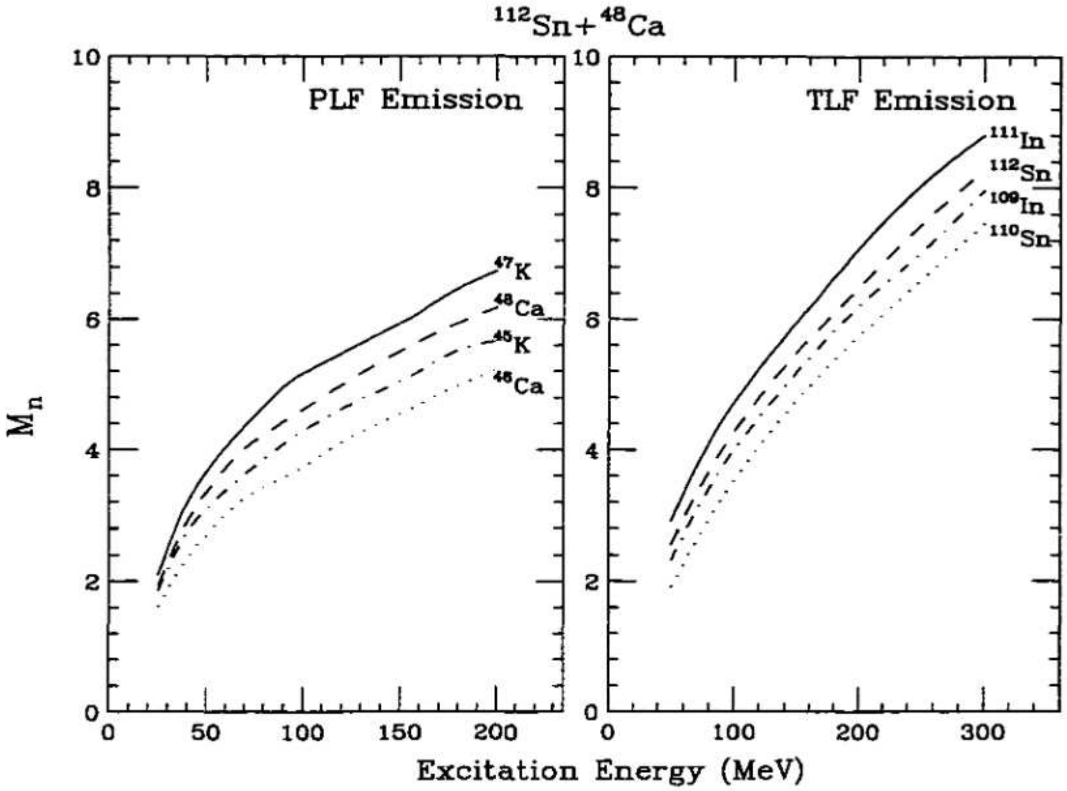

Figure 2.6: Gemini predictions of neutron multiplicity for emission from PLF (left panel) and emission from TLF (right panel) vs. its excitation energy, for ^{112}Sn + ^{48}Ca. Various curves represent a different (primary) projectile- or target-like fragment prior to the evaporation process.

not included in the earlier codes. The GEMINI code [CHA88a, CHA88b] developed by R.J.Charity, overcomes such deficiencies. This code provides a good description of the emission patterns and intensities for neutrons and light charged particles, even at Fermi energies, where excitation as high as 1 GeV have been observed.

The GEMINI code models the decay of an excited primary nuclei via sequential binary decays. All possible binary divisions, from light-particle emission to symmetric fission, in each decay step are considered. The computer code employs a Monte-Carlo technique to follow the decay chains of individual nuclei. This code employs the Hauser-Feshbach formalism [HAU52] for evaporation of the light fragments, ie., $Z \leq 2$, while for the decay of heavier fragments, it uses the transition state formalism of Moretto [MOR75] et al. Mathematical details can be found in the article by Charity [CHA88b] et al.

In the present work, GEMINI has been used for modeling the decay of excited primary projectile-like and primary target-like fragments from the ^{112}Sn + ^{40,48}Ca reactions. Since the excitation energies encountered in these reactions can be very high, the primary reaction fragments have a chance to lose a large fraction of their masses and charges. It is then not obvious, what can be learnt from the detectable secondary, post-evaporative fragments. Since the primary mass-to-charge density is an interesting degree of freedom, which is not directly accessible, the sensitivity of the statistical model predictions of neutron and proton yields on the primary fragment N/Z ratio was explored. Figs. 2.6 and 2.7 show the results of the model calculations, for the evaporation of protons and neutrons from the primary PLFs and TLFs.

Fig. 2.6 shows the Gemini predictions for the neutron multiplicity for emission from PLFs (left panel) and emission from TLFs (right panel), for ^{112}Sn + ^{48}Ca reaction at various excitation energies. The various curves represent particular primary projectile- or target-like fragments. One sees that the multiplicity of neutrons evaporated from the projectile- or target-like fragments is highly correlated with the excitation energy of the corresponding primary fragments. This correlation is almost linear for emission from heavier nuclei, ie., from the target-like fragments. Also, comparing the neutron yields from ^{47}K with those for ^{48}Ca, or the neutron yields from ^{111}In with those for ^{112}Sn, one notices that, on average, a primary fragment with larger N/Z ratio (^{47}K and ^{111}In) emits more neutrons during the decay process, even though the corresponding primary fragments have same number of neutrons. It is clearly demonstrated through such calculations that the total number of neutrons evaporated from an excited nucleus is sensitive to its N/Z ratio. However, experimentally it is difficult to measure such sensitivity, due to sizeable systematic errors in the measurement of neutron multiplicities. As shown further below, one can amplify the effects of primary fragments N/Z ratio by plotting the ratios of neutron-to-proton multiplicities, rather than the individual multiplicities.

Shown in Fig. 2.7 are the neutron-to-proton multiplicity ratios M_n/M_p, for emission from PLFs (left panel) and emission from TLFs (right panel), plotted vs. total excitation energy of the ^{112}Sn + ^{48}Ca system. Curves represent M_n/M_p ratios calculated for emission from projectile- or target-like fragments with N/Z equal to that of the projectile or target (solid curves) or that of the composite systems (dashed curves). Obviously, there are large differences observed in the ratio M_n/M_p for primary fragments with only small differences in N/Z. These differences are very large

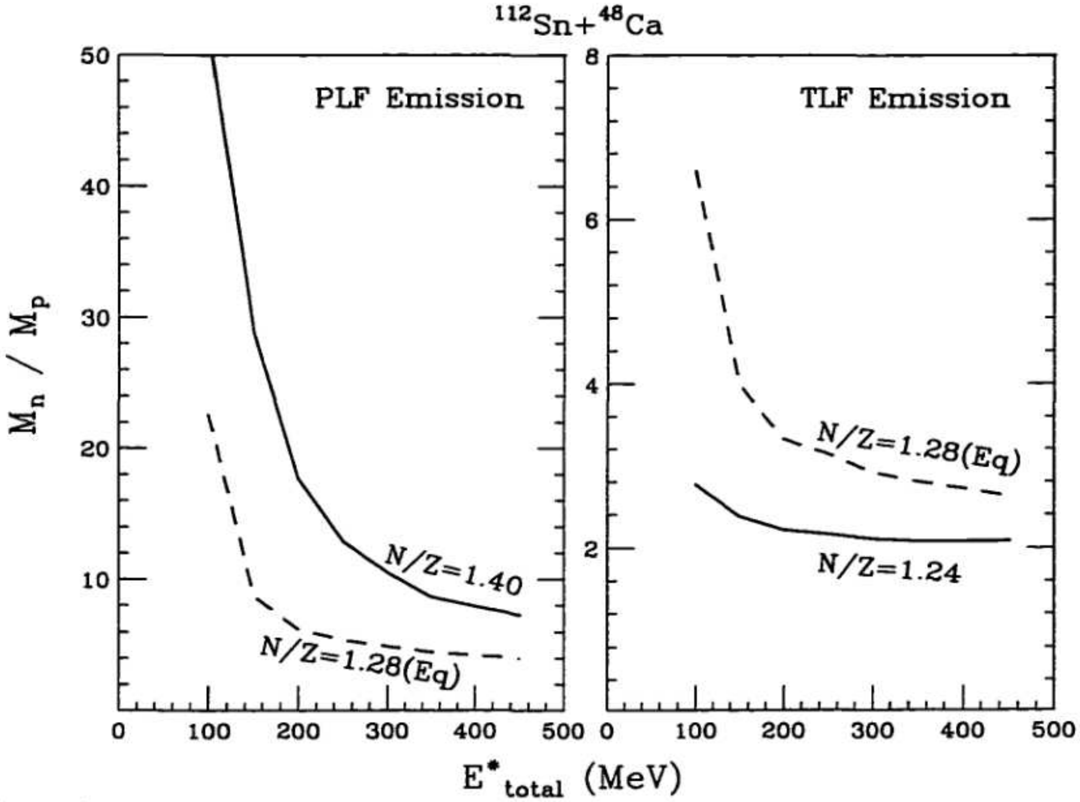

Figure 2.7: Gemini predictions of neutron-to-proton multiplicity ratio M_n/M_p for emission from PLFs (left panel) and emission from TLFs (right panel) vs. total excitation energy, for ^{112}Sn + ^{48}Ca. Curves represent M_n/M_p ratios calculated for emission from PLFs or TLFs with N/Z equal to that of the projectile or target (solid curves) or that of the composite systems (dashed curves).

for small excitation energies, as proton emission is suppressed due to the Coulomb barrier. Hence, the multiplicity ratio M_n/M_p is rather sensitive to the N/Z of the emitter, both for the lighter PLFs and the heavier TLFs. This sensitive analytical tool is used in the analysis of experimental results (see Chapter 5), to investigate the time evolution of the mass-to-charge asymmetry degree of freedom in the two systems studied.

2.3.2 Moving Source Parameterization

Information about the number of emitters, the total excitation energy, its division among different emitters, and the thermo-dynamical properties of these emitters can be extracted from the emission pattern of particles, even if the emitters disassemble completely. A schematic moving-source model has been very successful in the more quantitative task of discerning the number of emitters, their velocities, and thermo-dynamical characteristics from the random emission patterns for particles in

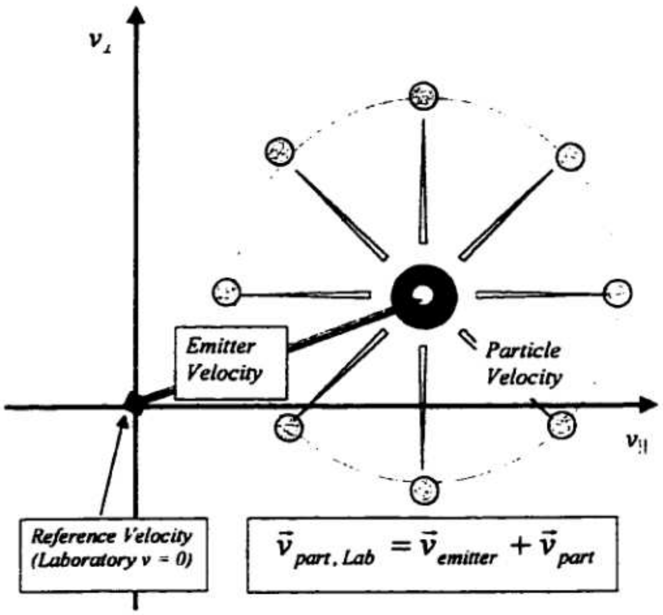
$v_\perp$
Emitter Velocity
Particle Velocity
$v_\parallel$
Reference Velocity (Laboratory v = 0)
$\vec{v}_{part,Lab} = \vec{v}_{emitter} + \vec{v}_{part}$

Figure 2.8: Pictorial representation of the random emission pattern in velocity space from a moving emitter. Particles emitted with a given constant speed but into random directions, from a moving emitter outline a circular yield pattern in laboratory velocity space, centered at the velocity of the emitter with a radius equal to the speed of the particles in the rest frame of the emitter.

the velocity space. As shown in Fig. 2.8, the particles emitted from a moving emitter with a given constant speed but into random directions, outline a circular yield pattern in laboratory velocity space, centered at the velocity of the emitter with a radius equal to the speed of the particles in the rest frame of the emitter. For each particle, the resultant velocity in the laboratory frame is a vector sum of the velocity of emitter in the laboratory and the velocity of the particle in emitter rest frame. Plotted in invariant form, also called galilei-invariant yield, the total yields, remain invariant under galilei-transformation, ie., they have same appearance in the laboratory frame and the rest frame of the emitter.

The double-differential yield for neutrons evaporated from an excited fragment in the emitter rest frame is well represented by a distribution of the following form

$$\frac{d^2 m_n}{(d\Omega_n.dE_n)_{rest}} = \frac{m_n}{4.\pi}.\left(\frac{1}{\Gamma(\alpha+1).\,\tau_s^{\alpha+1}}\right).\,E_n^{\alpha}.\,exp\left[\frac{-E_n}{\tau_s}\right] \tag{2.5}$$

where $\Gamma(\alpha{+}1)$ is the Γ function, τ_s is an effective nuclear temperature, m_n is the average neutron multiplicity. If on the average only one particle is evaporated, one has a Maxwellian spectrum with α=1 [$\Gamma(2)$=1], whereas for a neutron cascade, LeCoutour and Lang et. al. [LAN64, LEC59] have shown that α=0.45. It has also been demon-

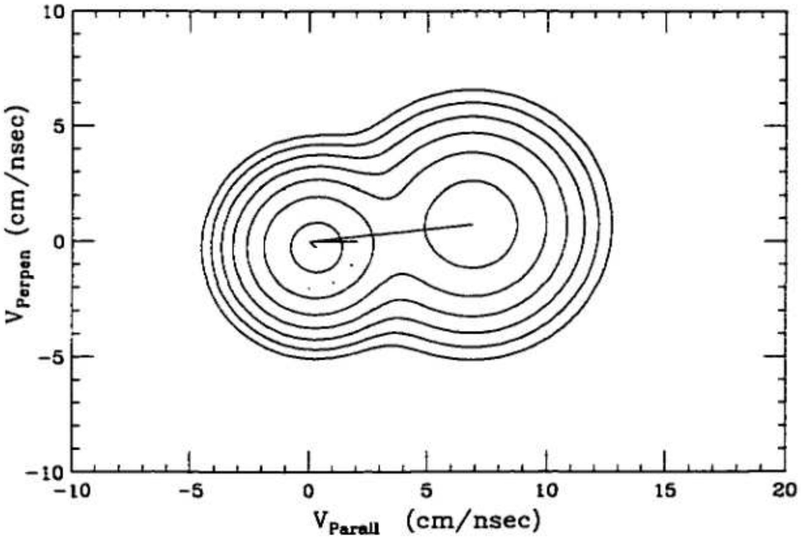

Figure 2.9: Similar to Fig. 2.8, showing a random emission pattern from two moving sources in velocity space. The velocities of two moving sources are represented by velocity vectors (the long and short one's) along with the velocity vector for the center-of-mass motion (intermediate length).

strated that evaporation spectra of fission neutrons can be described very well by using α=0.5 [$\Gamma(3/2)=\sqrt{\pi}/2$]. The effective temperature, τ_s, is related to the nuclear temperature (T) of the primary emitter. For a neutron cascade, $\tau_s = \frac{11}{12}$T.

The energy distribution of neutrons emitted from a thermally excited moving fragment, as described by equation 2.5 in the rest frame of the emitter, can be approximately described in the laboratory frame by the following equation,

$$\frac{d^2 m_n}{(d\Omega_n.dE_n)_{lab}} = \frac{m_n}{2}.\,(\pi.\tau_s)^{-3/2}.\,\sqrt{E_n}.\,exp[-(E_n - 2\sqrt{\epsilon_s.E_n}.\,cos(\theta_n) + \epsilon_s)/\tau_s] \quad (2.6)$$

Where E$_n$ is now the neutron laboratory energy, θ_n represents the laboratory neutron emission angle measured with respect to the direction of flight of the emitter, and ϵ_s is the kinetic energy per nucleon of the emitting source. For evaporation of a charged particle from a moving source, for example proton, the energy distribution can be described by a functional form very similar to equation 2.6, with only modification in the particle energy (E$_n$ → E$_p$ - E$_{Coulomb}$) for Coulomb repulsion. The exact expression for the galilei-invariant form equivalent to equation 2.6 can be found elsewhere [AWE82].

Fig. 2.9 is same as Fig. 2.8, however, it shows the yield for random and sequential emission of neutrons from two moving sources in form of contours. The velocities of two sources are represented by velocity vectors (the long and short one's) along with the velocity vector for the center-of-mass motion (intermediate one). The contour lines represent the galilei-invariant neutron yield as a function of velocity components parallel and perpendicular to the beam direction. At a given laboratory angle, the neutron energy spectrum can be obtained by projecting the invariant cross section for a cut through the distribution in that direction. The three dashes in Fig. 2.9 represent 30, 60, and 90 degrees, respectively in the laboratory frame. The corresponding neutron energy spectra at these angles are shown in Fig. 2.10.

Two components, shown in Fig. 2.10 as dotted and dashed curves, correspond to emission from the slow (target-like) and the fast (projectile-like) moving sources, while the solid curves represent the sum of both components. One notices that at forward angles, the yield is dominated by neutron emission from the fast-moving source, while at backward angles, the yield is mostly due to emission from the slow-moving source. Such total energy spectra (solid curve) comprising two distinct components, due to emission from two moving sources with very different velocities, can be well reproduced with fit functions defined by equation 2.6. From such fits, properties of the emitter, such as multiplicity, temperature, and velocity, can be extracted. The moving-source model is used further to simulate the more complex scenario of multiple sources with very different thermo-dynamical properties. Such scenario has been observed in experiments, attributed to sequential and fast-particle (prompt) emission modes. For example, two fully accelerated and equilibrated sources, the PLF and TLF sequentially emit particles, along with emission of particles which take place during early stages of collision, also known as prompt-particles or non-equilibrium particles, as they are emitted before any equilibrium is achieved.

Fig. 2.11 shows simple simulation calculations with the moving-source model for neutron emission in the reaction ^{112}Sn + ^{40}Ca, at a bombarding energy of 30 MeV/u and energy losses of $E_{loss} = 210$ and 400 MeV. In this figure, contour lines of the galilei-invariant neutron yields are plotted versus the neutron velocity components parallel and perpendicular to the beam direction. The continuous contour lines illustrate a situation in which neutron emission occurs only as sequential evaporation from the fully accelerated PLF and TLF. The total excitation energy was assumed to be divided approximately equally between PLF and TLF, leading to evaporative PLF

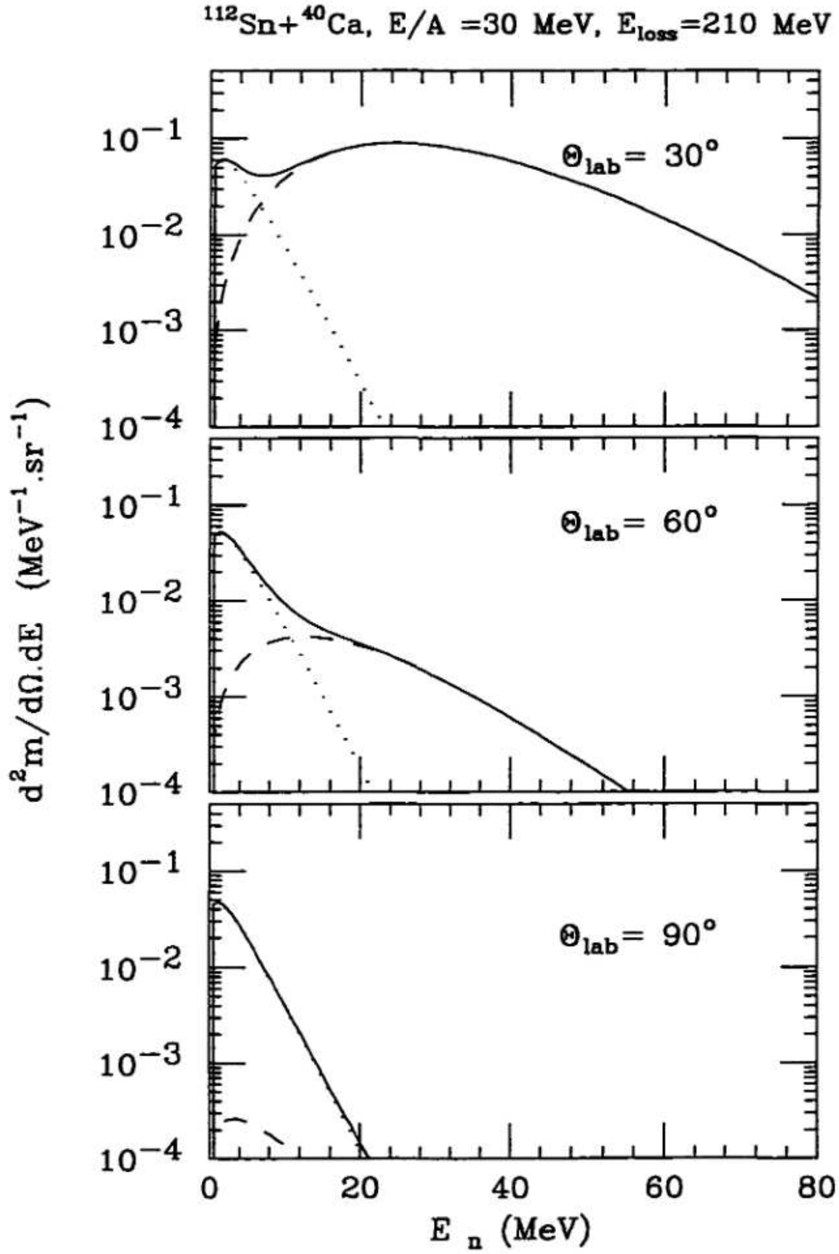

Figure 2.10: Plot of neutron energy spectra at three different laboratory angles. The two components, shown as dotted and dashed curves, correspond to emission from slow (target-like) and fast (projectile-like) moving sources shown in Fig. 2.9. Solid line represent the sum of two components.

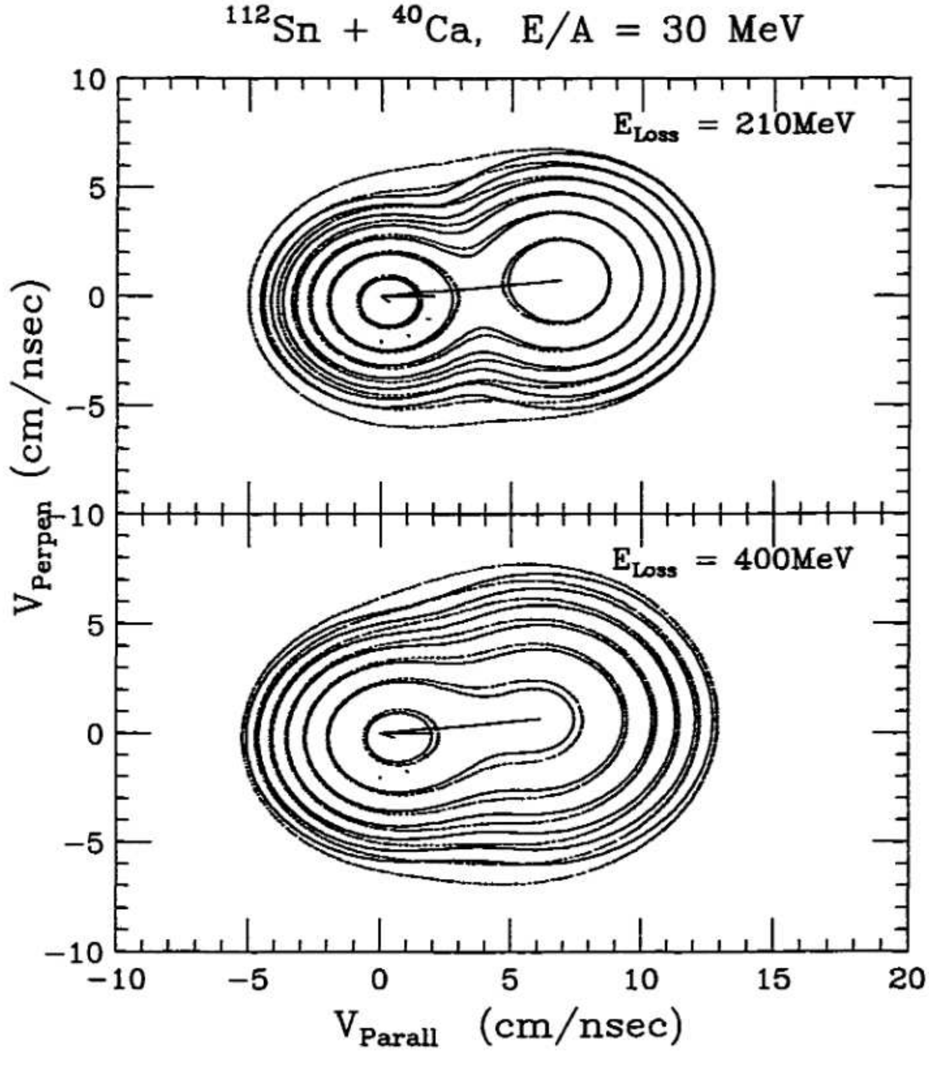

Figure 2.11: Plot of galilei-invariant neutron yields vs. the neutron velocity components parallel and perpendicular to the beam direction, for two different energy losses. The continuous contour lines are obtained assuming sequential emission from PLFs and TLFs, the dotted contour lines represent an added contribution from hypothetical non-equilibrium source.